UCSF
UC San Francisco Previously Published Works

Title

Mapping the orientation of nuclear pore proteins in living cells with polarized fluorescence microscopy

Permalink

https://escholarship.org/uc/item/9ck2h142

Journal

Nature Structural & Molecular Biology, 18(6)

ISSN

1545-9993

Authors

Kampmann, Martin
Atkinson, Claire E
Mattheyses, Alexa L
et al.

Publication Date

2011-06-01

DOI

10.1038/nsmb.2056

Peer reviewed

Mapping the orientation of nuclear pore proteins in living cells with polarized fluorescence microscopy

Martin Kampmann[1,2,4], **Claire E. Atkinson**[3], **Alexa L. Mattheyses**[3,4], and **Sanford M. Simon**[3]

[1]Laboratory of Cell Biology, The Rockefeller University, New York, New York 10065, USA

[2]Howard Hughes Medical Institute, The Rockefeller University, New York, New York 10065, USA

[3]Laboratory of Cellular Biophysics, The Rockefeller University, New York, New York 10065, USA

Abstract

The nuclear pore complex (NPC) perforates the nuclear envelope to facilitate selective transport between nucleus and cytoplasm. The NPC is composed of multiple copies of ~30 different proteins, termed nucleoporins, whose arrangement within the NPC is a major unsolved puzzle in structural biology. Various alternative models for NPC architecture have been proposed but not tested experimentally in intact NPCs. We present a method using polarized fluorescence microscopy to investigate nucleoporin orientation in live yeast and mammalian cells. Our results support an arrangement of both yeast Nic96 and human Nup133–Nup107 with their long axes approximately parallel to the nuclear envelope plane. This method can complement X-ray crystallography and electron microscopy to generate a high-resolution map of the entire NPC, and could monitor nucleoporin rearrangements during nucleocytoplasmic transport and NPC assembly. This strategy can also be adapted for other macromolecular machines.

INTRODUCTION

Understanding the mechanism of large macromolecular complexes is greatly facilitated by detailed knowledge of their structure. The elucidation of high-resolution structures of large complexes presents a unique challenge: high-resolution techniques, namely x-ray crystallography, can typically be applied only to individual proteins or smaller subcomplexes; conversely, techniques that are suitable for the study of the entire assembly, such as electron microscopy (EM), have limited resolution. Hence, structural information obtained from different techniques has to be integrated, which can be a formidable problem when the resolution gap between different types of structures is wide.

Correspondence should be addressed to martin.kampmann@ucsf.edu, catkinson@rockefeller.edu, mattheyses@emory.edu, simon@rockefeller.edu.
[4]Present addresses: Department of Cellular and Molecular Pharmacology and Howard Hughes Medical Institute, University of California at San Francisco, San Francisco, California 94158, USA (M.K.), Department of Cell Biology, Emory University School of Medicine, Atlanta, Georgia 30322, USA (A.L.M.).

A prime example of a macromolecular assembly that poses a "resolution-gap" problem is the nuclear pore complex (NPC), which mediates transport between the nucleus and the cytoplasm of eukaryotic cells (see ref. [1] for a recent review). The NPC is embedded in nuclear envelope pores and has a total mass of ~50 MDa in budding yeast and ~120 MDa in vertebrates. It is composed of ~30 distinct proteins, termed nucleoporins, which occur in multiple copies per NPC.

The structure of the NPC has been studied with different experimental approaches. EM has revealed the overall shape and symmetry of the NPC. Cryo-electron tomography has provided snapshots at a resolution better than 6 nm (ref. [2]). X-ray crystallography has elucidated high-resolution structures of an increasing number of individual nucleoporins and of some binary and ternary nucleoporin complexes[3]. However, the resolution of whole-NPC structures is currently not sufficient to relate high-resolution nucleoporin structures to the whole NPC by molecular docking. One approach to bridging this resolution gap is three-dimensional EM of NPC subcomplexes, followed by docking of nucleoporin crystal structures into the subcomplex EM map. This strategy revealed the arrangement of seven nucleoporins within the Y-shaped Nup84 subcomplex[4]. However, this approach has not yet resolved the higher-order arrangement of the Y-shaped subcomplex within the NPC.

The arrangement and orientation of nucleoporins within the NPC is therefore unknown. Several models for the arrangement of nucleoporins have been suggested. On the basis of immuno-EM and protein-protein interaction data, a coarse model for NPC architecture has been generated computationally[5]. However, this model lacks information regarding the orientation of NPC building blocks, which would be required for the docking of crystal structures into the overall map. On the basis of crystal structures and biochemical data, models have been proposed for the arrangement of two NPC building blocks, Nic96 and the Y-shaped subcomplex. For Nic96, an octameric ring arrangement has been proposed, in which the long axis of Nic96 is perpendicular to the nucleocytoplasmic axis[6]. For the Y-shaped subcomplex, two mutually exclusive models have been proposed: the "lattice" model[7,8] with the complex arranged around the NPC as a picket fence, and the "head-to-tail ring" model[9-11], for which the complex forms a ring around the pore. These models differ in the orientation of the Y-shaped subcomplex within the NPC. More generally, knowledge of the orientation of different nucleoporins within the NPC will be essential to determine the details of NPC architecture.

An experimental approach to mapping the orientation of nucleoporins within the NPC, either *in vitro* or *in vivo*, has not been described thus far. Here, we present a method for orientation mapping of nucleoporins in live yeast and mammalian cells using polarized fluorescence microscopy. Polarized fluorescence microscopy has previously been used to investigate macroscopically ordered systems of different geometries[12-17]. In particular, the anisotropy measured from a rigid tagging of GFP was used to monitor the orientation of septins in yeast cells[15,16]. We have recently used polarized fluorescence microscopy to probe the flexibility of nucleoporin domains in live cells[18].

We adapted and further developed these strategies to interpret information from polarized fluorescence microscopy in combination with known crystal structures of nucleoporins.

Using this approach, we obtained results that confirm the consensus model[6] for the arrangement of Nic96 in the budding yeast NPC and support the "head-to-tail ring" model, but not the "lattice" model for the 'Y-shaped' subcomplex in human cells. While designed to measure nucleoporin orientation, this method can be applied to investigate other protein assemblies in live cells.

RESULTS

Informative anisotropy patterns from NPC-fixed fluorophores

We set out to use polarized fluorescence microscopy to map the orientation of nucleoporins within the NPC. First, we derived an analytical description of how the variation in the anisotropy of a fluorescently tagged nucleoporin around the nuclear envelope depends on the orientation of the nucleoporin within the NPC. We defined a microscope-based coordinate system *xyz* such that *z* corresponds to the optical axis and *y* to the plane of polarization of the exciting light (Fig. 1a). We then defined a NPC-based coordinate system *NPQ* such that *N* is the nucleocytoplasmic axis and eightfold symmetry axis of an individual NPC, and *PQ* are parallel to the surrounding nuclear envelope; we chose *P* to coincide with *z* (Fig. 1b). When the cross-section of a spherical yeast nucleus is imaged by microscopy, the angle γ between *N* and *y* varies along the nuclear envelope cross-section (Fig. 1a). When a fluorophore is rigidly attached to a structured nucleoporin, the orientation of its transition dipole $\boldsymbol{\mu}$ is characterized by the angle α between *N* and $\boldsymbol{\mu}$ (Fig. 1b). Due to the symmetry constraints of the NPC, GFP molecules attached to nucleoporins present in eight or sixteen copies per NPC differ in their position around *N* (as indicated by angle β), but all share the same α.

We then calculated how α determines the anisotropy pattern of anisotropy, a measure of the polarization of light. Anisotropy is defined as:

$$Anisotropy\ r = \frac{I_{\parallel} - I_{\perp}}{I_{\parallel} + 2I_{\perp}} \quad \text{[Eq. 1]}$$

where $I_{\parallel}$ is the component of emitted light polarized parallel to the polarization of the exciting light, and $I_{\perp}$ is the perpendicular component. In the case of fluorophores attached to the NPC, the anisotropy will vary around the nuclear envelope cross-section as follows:

$$r(\gamma) = (K_2 - K_1) \frac{I_y - I_x}{(K_1 + 2K_2)I_x + (K_2 + 2K_1)I_y + 3K_3 I_z} \quad \text{[Eq. 2]}$$

where

$$I_x = \frac{1}{2}a^2c^2 + a^2d^2 + \frac{3}{8}b^2c^2 + \frac{1}{2}b^2d^2 - 2abcd \quad \text{[Eq. 3]}$$

$$I_y = a^4 + 3a^2b^2 + \frac{3}{8}b^4 \quad \text{[Eq. 4]}$$

$$I_z = \frac{1}{2}a^2\sin^2\alpha + \frac{1}{8}b^2\sin^2\alpha \quad \text{[Eq. 5]}$$

with $a = \cos\alpha\cdot\cos\gamma$, $b = \sin\alpha\cdot\sin\gamma$, $c = \sin\alpha\cdot\cos\gamma$ and $d = \cos\alpha\cdot\sin\gamma$.

Our derivation of equations 2-5 is given in the Supplementary Note. K_1, K_2 and K_3 are correction factors for high numerical aperture observation[13]. Equation 2 is displayed in Figure 1c. As expected from the symmetry of the NPC/nuclear envelope system, $r(\gamma)$ has a periodicity of 180° and displays mirror symmetry around the axes $\gamma = 90°$, $\gamma = 180°$ and $\gamma = 270°$.

While experimentally measured anisotropy values differ from the theoretical values (Supplementary Note), the overall anisotropy pattern is less sensitive to experimental factors. Three types of anisotropy patterns are predicted, as illustrated in Figure 1d: type I, displaying maxima for $\gamma = 0°$ and 180° and minima for $\gamma = 90°$ and 270°, type II, displaying minima for $\gamma = 0°$, 90°, 180°, and 270° alternating with maxima, and type III, with minima for $\gamma = 0°$ and 180° and maxima for $\gamma = 90°$ and 270°.

The α-values at which transitions between pattern types occur are shown in Fig. 1e. The dependence on α is relatively robust with respect to experimental error. Photobleaching does not affect anisotropy measurements in our setup (Supplementary Fig. 1a), however, experimental factors affecting the measured anisotropy values include the resolution of the microscope in the z-direction, averaging of pixels with different γ-values during image processing, and fluorophore flexibility. As described in the Supplementary Note, these experimental factors cause flattening of the measured anisotropy curves, which can be approximated by convolution of the theoretical anisotropy curves with a Gaussian function (Supplementary Fig. 1b). The exact width of this Gaussian function is unknown, but over the range of widths tested, even very wide Gaussian functions changed the boundaries between pattern types only over a narrow range of α-values (Fig. 1e). Therefore, we can make the following very conservative assumptions about α based on the observed pattern type: Type I: 0° $\alpha < 42°$; Type II: 33 α 68°; Type III: 60° < α 90°.

Furthermore, the amplitude of $r(\gamma)$ within one pattern type changes monotonically with α. Hence, when comparing two anisotropy patterns of the same type with different amplitudes, acquired for different nucleoporin–fluorophore constructs under the same experimental conditions, it is always possible to determine which construct has a relatively higher α value.

In summary, we can gain information about the orientation of the dipole of a fluorophore fixed within the NPC by examining the pattern of anisotropy maxima and minima around the nuclear envelope cross-section. However, the biological parameter of interest is the orientation of nucleoporins within the NPC, and not the orientation of the fluorophore itself. The spatial relation of a fluorophore to a nucleoporin can be formalized as shown in Figure 1f: Two perpendicular axes, u and v, are arbitrarily defined within the nucleoporin. ω and θ are the angles between μ and u, and μ and v, respectively. The orientation of the nucleoporin within the NPC is characterized by two angles (Fig. 1g): ψ, the angle between u and N, and

ϕ, describing rotation of the ***v*** around ***u***. We show below how to derive information about ψ and ϕ from anisotropy patterns.

Functional Nic96–GFP fusion proteins with known geometry

To map the orientation of nucleoporin–GFP fusion constructs within the, rigid constructs with known geometry are required. To this aim, we adapted a previously published approach[15]: GFP contains a short N-terminal α-helix, which can be fused directly to a C-terminal α-helix in a protein of interest to link the two proteins by a continuous α-helix. When the number of amino acids in this linker helix is varied, GFP rotates around the linker helix axis by angles dictated by α-helical geometry[16]. For GFP, the orientation of the fluorescence transition dipole relative to its crystal structure has been previously determined[19]. Therefore, the orientation of the dipole with respect to the nucleoporin can be predicted based on the length of the linker helix. In our nomenclature, a fusion construct is described two numbers, $(-p/-q)$, indicating the number of amino acids omitted from the C-terminus of the nucleoporin (p) and the number of amino acids omitted from the N-terminus of GFP (q). Different constructs for which the sum of p and q is the same have a linker helix of the same length.

The first nucleoporin we chose to investigate was yeast Nic96, since a model has been proposed for its orientation in the NPC[6], which makes Nic96 a good test case for our method. Nic96 contains C-terminal α-helices, and crystal structures for its C-terminal domain are available[6,20], which allowed us to generate molecular models for Nic96–GFP fusion constructs (Fig. 2). Since Nic96 is an essential protein in yeast, we could assay whether a given Nic96–GFP construct was functional *in vivo* (Supplementary Fig. 2a). Molecular models for some nucleoporin–GFP fusion constructs contain internal steric clashes between the nucleoporin and GFP moieties (red stars in Supplementary Fig. 2a). Thus, these constructs cannot exist in the modeled conformations, and when they were expressed in yeast, they had reduced or no function as assayed by tetrad analysis, and the GFP fluorescence lacked a clear nuclear localization (Supplementary Fig. 2). These constructs, as well as other constructs with drastically reduced Nic96 function and/or reduced nuclear-envelope staining were excluded from further analysis. The six Nic96–GFP constructs that passed all tests were $(-5/-4)$, $(-6/-4)$, $(-5/-5)$, $(-8/-5)$, $(-21/-4)$ and $(-20/-5)$.

Anisotropy patterns support model for Nic96 arrangement

We collected $I_{\parallel}$ and $I_{\perp}$ images of GFP-labeled cells in parallel with an optimized microscope setup (details are described in the Methods section). To calculate accurate anisotropy values pixel-by-pixel, precise alignment of the $I_{\parallel}$ and $I_{\perp}$ images was necessary, especially since the nuclear envelope signal was only few pixels wide. Global alignment of the $I_{\parallel}$ and $I_{\perp}$ halves of the micrograph did not give satisfactory results for all cells. We therefore cropped image pairs of individual nuclei from the micrographs (Fig. 3a), and aligned all images automatically with sub-pixel accuracy based on cross-correlation. Intensity-based thresholding of each image pair to exclude pixels that did not represent the nuclear envelope was also more accurate on a nucleus-by-nucleus basis. The nucleus was automatically centered within the image, using a center-of-gravity algorithm, and the

anisotropy image was calculated from background-corrected aligned $I_\parallel$ and $I_\perp$ images. The image was divided into 32 segments and the anisotropy values within each segment were recorded (Fig. 3a).

The resulting anisotropy patterns were averaged over all nuclei (Fig. 3b). All patterns were type I, but the amplitudes of the (−5/−4) and (−8/−5) patterns were higher than those of the other patterns. While all patterns in the case of the Nic96–GFP constructs were type I, this was not true of all yeast nucleoporins: a series of Nup84–GFP constructs showed a different combination of pattern types (Supplementary Figure 3),

To interpret the anisotropy measurements for Nic96–GFP constructs, we defined axes $\boldsymbol{u}$ and $\boldsymbol{v}$ within Nic96 as shown in Figure 4a. $\boldsymbol{u}$ corresponds to the long axis of the crystallized Nic96 domain. Since constructs (−6/−4) and (−5/−5) have the same linker helix length, as do constructs (−21/−4) and (−20/−5), we generated four distinct molecular models for the six constructs (Fig. 2). From each model, angles θ and ω were determined. As detailed in the Supplementary Note, this allowed us to calculate for each construct the value of α we expect for any combination of ψ and ϕ (Fig. 4b, *first row*).

We then used these construct-specific plots of α as a function of ψ and ϕ to identify the range of ψ and ϕ values that was compatible with the anisotropy patterns we observed. As described in the previous section, our conservative assumption is that type I anisotropy patterns occur for constructs with $\alpha < 42°$. Since we observed type I patterns for all constructs, we could restrict the space of possible ψ and ϕ combinations in each plot to those values that correspond to $\alpha < 42°$ (Fig. 4b, *second row*).

We could further define possible ψ and ϕ combinations by comparing the amplitudes between pairs of anisotropy patterns for the different constructs (Fig. 4b, *third row*). For two constructs with type I patterns, the construct with the higher amplitude will have the lower value of α. For example, the amplitude for Nic96–GFP (−5/−4) was larger than for Nic96–GFP (−6/−4), Nic96–GFP (−5/−5), Nic96–GFP (−21/−4) and Nic96–GFP (−20/−5). Therefore, only combinations of ψ and ϕ for which Nic96–GFP (−5/−4) had smaller α-values than the other four constructs were compatible with our data.

By combining all these conditions, we can restrict ψ to values between 77° and 90° and ϕ to values between 20° and 45° (Fig. 4b, *bottom row*). Notably, the high value of ψ indicates that the long axis of Nic96 is close to perpendicular to the nucleocytoplasmic axis of the NPC (Fig. 4c), as predicted by the published model for the arrangement of Nic96 within the NPC[6].

To validate our method, we applied it to a different biological system, the vacuolar ATPase. This protein complex is embedded in the membrane of the yeast vacuole, a large, spherical organelle. The vacuolar ATPase/vacuole system and the NPC–nuclear envelope system thus have similar geometries. GFP-tagging of a vacuolar ATPase subunit with known orientation resulted in the anisotropy pattern predicted by our approach (Supplementary Fig. 4), thus confirming the general applicability of the approach.

Nup133–GFP supports Y-shaped complex "head-to-tail ring"

A question of major biological interest is the orientation of the Y-shaped subcomplex within the NPC[7-11]. We decided to study the Y-shaped subcomplex from mammalian cells (the Nup107/160 complex), rather than the homologous subcomplex from yeast (the Nup84 complex), since no crystal structure containing a C-terminal α-helix is currently available for members of the yeast Y-shaped complex. Structures of the C-terminal domains of two members of the human Y-shaped complex, Nup107 and Nup133, have been published[21-23]. Several Nup133–GFP constructs (Supplementary Fig. 5) localized to the nuclear envelope in Hela cells (Fig. 5a), whereas none of the tested Nup107–GFP constructs did.

While anisotropy patterns can be observed for Nup133–GFP constructs in individual HeLa cells (Fig. 5b), automated quantification of r as a function of γ had to be modified from the yeast algorithm, since nuclei of mammalian cells are not as spherical as yeast nuclei. We cropped small regions of quasi-linear nuclear envelope segments from each micrograph (Fig. 5c) and determined the orientation of each segment automatically by cross-correlation based matching between the experimental image and synthetic template images representing orientations of γ between 0° and 180° in 10° increments (Fig. 5d). The average anisotropy was calculated as for yeast cells, and anisotropy graphs were plotted (Fig. 5e). The experimental anisotropy graphs for mammalian cells cover a range of $0° < \gamma < 180°$, which is sufficient to interpret the anisotropy pattern, due to the 180°-periodicity of $r(\gamma)$.

We analyzed four Nup133–GFP constructs for which the molecular models showed no internal steric clashes (Supplementary Fig. 5). Constructs (−2/−5) and (−3/−4) have a linker helix with the same length, as do constructs (−3/−5) and (−4/−4). Constructs (−2/−5) and (−3/−4) showed a type I anisotropy pattern. The anisotropy curves for constructs (−3/−5) and (−4/−4) are relatively noisy, but the presence of a clear maximum at $\gamma = 90°$ is the hallmark of a type III anisotropy pattern (compare to Fig. 1d).

Based on the structure of a complex between the C-terminal domains of Nup107 and Nup133, we defined $\boldsymbol{u}$ as the axis between the N-terminal residues of the Nup107 and Nup133 constructs, thus pointing towards the remaining residues of the two nucleoporins (Fig. 6a). On the basis of the structure of the homologous yeast Nup84 complex[4], we assume that Nup107 and Nup133 are arranged linearly along the stem of the Y-shaped subcomplex. Hence, $\boldsymbol{u}$ is likely to reflect the orientation of the stem of the Nup107 complex.

Maps of α as a function of φ and ψ were created for the Nup133–GFP constructs (Fig. 6b, *first row*) as described for the yeast constructs. Based on the observed anisotropy patterns, our conservative assumptions were $\alpha < 42°$ for constructs (−2/−5) and (−3/−4) (type I pattern) and α > 60° for constructs (−3/−5) and (−4/−4) (type III pattern) (Fig. 6b, *second row*). These conditions restricted the values of ψ to values between 76° and 90° and φ to values between 36° and 90° (Fig. 6b, *bottom row*), indicating that the long axis of the Nup107–Nup133 dimer, which is likely to represent the stem axis of the entire subcomplex, lies approximately perpendicular to the nucleocytoplasmic axis of the NPC. Such an arrangement is compatible with the "head-to-tail ring" model, in which the Y-shaped subcomplexes lie with their long axis parallel to the nuclear envelope plane and form a ring through interaction of the end of the stem of the 'Y' with the short arms of the neighboring

'Y'[9] (Fig. 6c and Supplementary Fig. 6a). However, the anisotropy patterns are not compatible with the "lattice" model as originally proposed, or any other models in which the Y-shaped subcomplexes interact via their short arms, with their long axes parallel to the nucleocytoplasmic axis[8] (Supplementary Fig. 6b). The same answer is obtained by asking which anisotropy pattern types we would expect to observe on the basis of the alternative models for the arrangement of the Y-shaped complex in the NPC (Supplementary Fig. 6d).

DISCUSSION

We have developed a method to map the orientation of nucleoporins within the NPC of live yeast and mammalian cells. The development of this method required us to address several technical challenges. To acquire micrographs with a sufficient signal-to-noise ratio despite the low abundance of nucleoporins in yeast, we optimized cell culture conditions to minimize cellular background fluorescence. In addition, we computationally corrected for the remaining background fluorescence. To cleanly separate $I_{\parallel}$ and $I_{\perp}$ light components, we customized our microscope setup using a laser, a half-wave plate, and clean-up polarizers. To align $I_{\parallel}$ and $I_{\perp}$ images with sub-pixel accuracy, we developed a cross-correlation based algorithm.

Several caveats in the interpretation of anisotropy patterns needed to be considered. As in all GFP-tagging experiments, a primary concern is that the GFP tag could disrupt the structure and localization of the tagged protein. To exclude such disruptive nucleoporin–GFP constructs from our analysis, we applied a combination of three criteria to each construct in yeast: (i) the molecular model of the nucleoporin–GFP construct had to be free of steric clashes, (ii) the construct needed to show a robust nuclear envelope localization *in vivo*, and (iii) the nucleoporin–GFP had to be functional *in vivo*. In the case of an essential nucleoporin, such as Nic96, viability of cells in which Nic96–GFP replaces wild-type Nic96 can directly be assayed (Supplementary Fig. 2a). For non-essential nucleoporins, function can be assayed in a genetic background lacking a second gene that is synthetic lethal with the nucleoporin of interest. We found that the three criteria were correlated for most Nic96–GFP constructs (Supplementary Fig. 2). Only constructs satisfying all three criteria were used for further analysis. The first two criteria were applied to mammalian cells as well.

A second caveat is the experimental error in the anisotropy values (discussed in the Supplementary Note). We overcame this issue by relying on anisotropy pattern types, rather than absolute anisotropy values, for our analysis. Our conclusions based on anisotropy patterns were extremely conservative (Supplementary Note), yet they efficaciously restricted the space of possible nucleoporin orientations (Figs. 4 and 6). The observation that the results from all of the nucleoporin–GFP constructs we investigated were consistent with each other supports the validity of our approach.

The third caveat is that the *in vivo* conformation of a nucleoporin–GFP fusion construct may differ from the conformation predicted by the molecular model. While short α-helices are very stiff in isolation (persistence length ~100 nm, ref. [24]), interactions with other molecular surfaces in the NPC may bend the linker helix. This possibility is difficult to exclude experimentally, since even a crystal structure of the nucleoporin–GFP construct may not

reflect the geometry adopted in the context of the NPC. However, our results support the conclusion that the molecular model was generally an adequate description of the nucleoporin–GFP geometry: (i) Different constructs with the same linker helix length, and thus the same predicted geometry produced indistinguishable anisotropy patterns; a small divergence was only observed in the case of Nic96–GFP (−5/−5) and (−6/−4). (ii) Conclusions from all individual constructs were consistent with each other: anisotropy patterns never resulted in mutually exclusive predictions of ϕ and ψ. (iii) Models derived from our analysis are consistent with NPC dimensions. In particular, the conclusion that the long axis of the Y-shaped subcomplex is close to perpendicular to the nucleocytoplasmic axis is compatible with the size of the central NPC, whereas an arrangement of the subcomplex with its long axis (~45 nm long[4]) parallel to the nucleocytoplasmic axis would exceed the height of one half of the central NPC (~15–20 nm, ref. [2]). (iv) Models that did not show steric clashes both localized properly at the nucleus and could complement loss of the endogenous gene, whereas this was not true of those constructs that were predicted to contain a steric clash. The fact that yeast cells expressing nucleoporin–GFP constructs with predicted steric clashes had generally reduced viability supports the idea that the nucleoporin–GFP linkage is rather rigidly dictating the structure of the fusion construct, and not easily altered by other external factors.

The method we describe here can be applied to all nucleoporins that feature an α-helical C-terminal domain. According to secondary structure predictions, ~60% of nucleoporins meet this requirement[25]. While it should be possible to collect anisotropy data for all of these nucleoporins, a crystal structure of the C-terminal domain is required to derive orientation information from the anisotropy patterns. If the elucidation of nucleoporin crystal structures progresses at the current pace[3], our method should help to map the orientation of most NPC components over the next few years. This experimental determination of nucleoporin orientations will complement crystallographic and EM data in the construction of a high-resolution map of the entire NPC, which will be the basis of a detailed mechanistic understanding of the NPC.

Since the present method is applied to live cells, it can be used to monitor changes in nucleoporin orientation that correlate with NPC assembly and transport. Structural studies suggest that even the ordered components of the NPC are highly dynamic[2,4,26], but the biological significance of this flexibility is unclear, since it has not been studied in intact cells. Using small-molecule inhibitors of nucleocytoplasmic transport or temperature-sensitive transport mutants, NPCs can be arrested in an inactive state[27], and nucleoporin orientations in the inactive state can be compared to the active state to reveal conformational changes that occur specifically during active transport. Time-resolved studies of NPC assembly can yield insights into nucleoporin rearrangements during the assembly process.

Finally, our method can be adapted to study systems other than the NPC, as long as the system has the following properties: (i) The system is oriented with respect to a larger cellular structure, such as the plasma membrane or ordered cytoskeletal structures, (ii) A crystal structure containing a C-terminal α-helix is known for at least one component of the system, and (iii) the local concentration of the macromolecular complex is high enough to collect data with a sufficient signal-to-noise ratio. Note that while the NPC is a highly

symmetrical structure, this is not a requirement for the application of the present method. While the extreme C-terminus of many proteins may consist of a small number of disordered residues, these residues can be trimmed to fuse the GFP to the most C-terminal α-helix, as we have demonstrated here for Nic96.

One example of a different biological system is the vacuolar ATPase (Supplementary Fig. 4), and another potential example is co-translational protein translocation into the endoplasmic reticulum (ER). The rough ER is continuous with the outer nuclear envelope, which is densely covered with ribosomes engaged in co-translational translocation. Since the cytoplasmic-luminal axis of the protein-conducting channel/ribosome system is always perpendicular to the surface of the nuclear envelope segment it is attached to, the average steady-state orientation of different GFP-tagged components of the system can be determined exactly as for the NPC.

METHODS

Yeast strains

Saccharomyces cerevisiae W303a and W303α cells (American tissue culture collection) were transformed with the BglII fragment of pRS422 (ref. [28]) containing the ADE2 gene. Adenine-prototroph transformants were selected and crossed to obtain the diploid MKY363. Nucleoporins and Tfp1 were genomically tagged with EGFP in MKY363 with standard methods[29], using the primers listed in the Supplementary Table and the template plasmids pKT127 and pKT128 (ref. [29]). The identity of the different Nic96–GFP strains was confirmed by sequencing of the genomic DNA junction region between Nic96 and GFP, using the control primers listed in the Supplementary Table. Sporulation and tetrad dissection of diploid cells followed standard procedures[30].

Construction of nucleoporin–GFP plasmids for expression in mammalian cells

In a first PCR, the EGFP coding sequence was amplified from plasmid pEGFP-C1 (Clontech) using primers GFP-f and GFP-NotI-r (Supplementary Table), introducing a NotI site downstream of the stop codon. In a second PCR, a fragment of the Nup133 coding sequence was amplified from plasmid MHS1010-58232 (Open Biosystems) and the junction with the EGFP sequence was introduced using the forward primer Nup133-f and different reverse primers for the different Nup133–GFP constructs (Supplementary Table). In a third PCR, products from the first two PCRs were used as templates with primers Nup133-f and GFP-NotI-r to fuse the Nup133 fragment to the full-length GFP sequence. The product of this PCR and plasmid MHS1010-58232 were digested with PflFI and NotI, and the PCR product was ligated into the larger background fragment from the MHS1010-58232 digest to obtain Nup133–GFP expression plasmids. The sequence of the insert was verified by sequencing with primers M13-Forward(−20), Nup133-f, Nup133–GFP-seq-1, Nup133–GFP-seq-2, and Nup133–GFP-seq-3 (Supplementary Table).

Microscopy

Images were collected on an Olympus IX-70 microscope with a 1.45NA 60× objective lens (Olympus, Center Valley, PA), using light from a 488-nm argon laser (Spectra Physics -

now Newport, Irvine CA) passed through a polarizer (Chroma, Bellows Falls, VT) and a half wave plate (ThorLabs, Newton NJ). A 535/30ET emission filter (Chroma) and 500LP dichroic (Chroma) were used and the components of the emitted light parallel and perpendicular to the direction of polarization of the exciting light were separated by an Optosplit III splitter (Cairn, Kent UK) containing a polarizer (Chroma), passed through clean-up polarizers (Chroma) and simultaneously recorded side by side with an Orca ER camera (Hamamatsu, Hamamatsu City, Japan). Image acquisition was software-controlled (Metamorph). *Yeast*. To minimize background fluorescence, yeast cells were grown exponentially for 24 hours by sequential dilution in low-fluorescence medium[29] at 30°C. For imaging, diploid cells from 1–3 ml of culture were resuspended in a small amount of low-fluorescence medium, 1 μl was dispensed onto a glass slide, and a cover slip (Number 1.5, VWR) was applied with slight pressure. Images were collected at room temperature with 2000 ms exposure time. *Mammalian Cells*. HeLa cells were grown in DMEM (GIBCO) containing penicillin, streptomycin and fetal bovine serum (GIBCO) in 35-mm glass bottom dishes (No. 1.5, MatTek, Ashland MA). Cells were transfected with Nup133–GFP expression plasmids using lipofectamine (Invitrogen), following the manufacturer's protocol. Cells were imaged 18–48 hours after transfection in CIM (Hanks BBS (Sigma) containing 5% fetal bovine serum and 10 mM HEPES pH 7.4) at 37°C with 2000 ms exposure time.

Computational image analysis

Background subtraction: Images of cells were corrected for growth medium fluorescence by subtracting an image of medium. Images of individual nuclei were cropped from micrographs, and the cytoplasmic background for each cell was subtracted. *Anisotropy compensation*: The difference in light transmission between the parallel and perpendicular channels was corrected using images of aqueous fluorescein solution (Sigma) for which we assumed an anisotropy of 0. We applied objective correction factors developed by Axelrod[13] as detailed in the Supplementary Note. *Image Alignment*: Images from the parallel and perpendicular channels were aligned with sub-pixel accuracy based on cross-correlation in SPIDER[31]. *Yeast*: the remaining processing steps were implemented in Matlab (The Mathworks). An anisotropy image was calculated from the aligned parallel and perpendicular images according to the definition of anisotropy (Eq. 1). To mask pixels outside the nuclear envelope, only the 10% brightest pixels in a sum image of the parallel and perpendicular channels were included in further analysis. The image was divided in 32 sectors, each corresponding to an angle of 11.25°, and the average anisotropy was calculated for all pixels from all cells falling within this sector, and the standard deviation was calculated. *Mammalian cells*: 16×16 pixel images of nuclear envelope segments were cropped from micrographs. In SPIDER, the cross-correlation was calculated between these segments and 18 artificial images of a line with different orientations, as shown in Figure 5d. Each image was assigned to the most similar template. Only pixels with intensities at least one standard deviation above the average pixel intensity were included in the further analysis. The average anisotropy was calculated for each image. For all images aligned to one template, the average anisotropy and standard deviation were calculated.

Molecular models

Models of fusion proteins were built in UCSF Chimera[32] from the following crystal structures: EGFP, PDB 1EMG[33]; Nic96, PDB 2QX5 (ref. [20]); Nup133–Nup107, PDB 3I4R[23]; Tfp1, PDB 1VDZ[34]. GFP was positioned with respect to the tagged protein such that the linker helix was continuous. Vectors were calculated from PDB coordinates: $\boldsymbol{\mu}$, vector between fluorophore atoms CE1 and O2; Nic96-$\boldsymbol{u}$, vector between Trp334-CA and Ile723-CG1; Nic96-$\boldsymbol{v}$, vector normal to Nic96-$\boldsymbol{u}$ passing through Leu200-N; Nup133-Nup107-$\boldsymbol{u}$, vector between Nup107-Glu667-CA and Nup133-Lys518-CA; Nup133-Nup107-$\boldsymbol{v}$, vector normal to Nup133-Nup107-$\boldsymbol{u}$ passing through Nup133-Ile1156-CA; Tfp1-$\boldsymbol{u}$, vector between Val521-C and Gln191-OE1. Angles θ and ω for each construct were calculated from these vector coordinates. From these, maps of α as a function of ϕ and ψ were calculated in Matlab as detailed in the Supplementary Note. The following EM structures were used: EMDB-5152 (ref. [4]) for Fig. 6C and Supplementary Figure 6; EMDB-1640 (ref. [35]) for Supplementary Figure 4. Registration of the yeast Tfp1 sequence with PDB 1VDZ was determined using FUGUE[36].

Supplementary Material

Refer to Web version on PubMed Central for supplementary material.

Acknowledgments

References

1. Lim RY, Ullman KS, Fahrenkrog B. Biology and biophysics of the nuclear pore complex and its components. Int Rev Cell Mol Biol. 2008; 267:299–342. [PubMed: 18544502]

2. Beck M, Lucic V, Forster F, Baumeister W, Medalia O. Snapshots of nuclear pore complexes in action captured by cryo-electron tomography. Nature. 2007; 449:611–5. [PubMed: 17851530]

3. Brohawn SG, Partridge JR, Whittle JR, Schwartz TU. The nuclear pore complex has entered the atomic age. Structure. 2009; 17:1156–68. [PubMed: 19748337]

4. Kampmann M, Blobel G. Three-dimensional structure and flexibility of a membrane-coating module of the nuclear pore complex. Nat Struct Mol Biol. 2009; 16:782–8. [PubMed: 19503077]

5. Alber F, et al. The molecular architecture of the nuclear pore complex. Nature. 2007; 450:695–701. [PubMed: 18046406]

6. Schrader N, et al. Structural basis of the nic96 subcomplex organization in the nuclear pore channel. Mol Cell. 2008; 29:46–55. [PubMed: 18206968]

7. Brohawn SG, Schwartz TU. Molecular architecture of the Nup84-Nup145C-Sec13 edge element in the nuclear pore complex lattice. Nat Struct Mol Biol. 2009; 16:1173–7. [PubMed: 19855394]

8. Brohawn SG, Leksa NC, Spear ED, Rajashankar KR, Schwartz TU. Structural evidence for common ancestry of the nuclear pore complex and vesicle coats. Science. 2008; 322:1369–73. [PubMed: 18974315]

9. Seo HS, et al. Structural and functional analysis of Nup120 suggests ring formation of the Nup84 complex. Proc Natl Acad Sci U S A. 2009; 106:14281–6. [PubMed: 19706512]

10. Debler EW, et al. A fence-like coat for the nuclear pore membrane. Mol Cell. 2008; 32:815–26. [PubMed: 19111661]

11. Hsia KC, Stavropoulos P, Blobel G, Hoelz A. Architecture of a coat for the nuclear pore membrane. Cell. 2007; 131:1313–26. [PubMed: 18160040]

12. Ajtai K, Toft DJ, Burghardt TP. Path and extent of cross-bridge rotation during muscle contraction. Biochemistry. 1994; 33:5382–91. [PubMed: 8180161]

13. Axelrod D. Carbocyanine dye orientation in red cell membrane studied by microscopic fluorescence polarization. Biophys J. 1979; 26:557–73. [PubMed: 263688]

14. Rocheleau JV, Edidin M, Piston DW. Intrasequence GFP in class I MHC molecules, a rigid probe for fluorescence anisotropy measurements of the membrane environment. Biophys J. 2003; 84:4078–86. [PubMed: 12770911]

15. Vrabioiu AM, Mitchison TJ. Structural insights into yeast septin organization from polarized fluorescence microscopy. Nature. 2006; 443:466–9. [PubMed: 17006515]

16. Vrabioiu AM, Mitchison TJ. Symmetry of septin hourglass and ring structures. J Mol Biol. 2007; 372:37–49. [PubMed: 17628594]

17. Corrie JE, et al. Dynamic measurement of myosin light-chain-domain tilt and twist in muscle contraction. Nature. 1999; 400:425–30. [PubMed: 10440371]

18. Mattheyses AL, Kampmann M, Atkinson CE, Simon SM. Fluorescence anisotropy reveals order and disorder of protein domains in the nuclear pore complex. Biophys J. 2010; 99:1706–17. [PubMed: 20858414]

19. Rosell FI, Boxer SG. Polarized absorption spectra of green fluorescent protein single crystals: transition dipole moment directions. Biochemistry. 2003; 42:177–83. [PubMed: 12515552]

20. Jeudy S, Schwartz TU. Crystal structure of nucleoporin Nic96 reveals a novel, intricate helical domain architecture. J Biol Chem. 2007; 282:34904–12. [PubMed: 17897938]

21. Berke IC, Boehmer T, Blobel G, Schwartz TU. Structural and functional analysis of Nup133 domains reveals modular building blocks of the nuclear pore complex. J Cell Biol. 2004; 167:591–7. [PubMed: 15557116]

22. Boehmer T, Jeudy S, Berke IC, Schwartz TU. Structural and functional studies of Nup107/Nup133 interaction and its implications for the architecture of the nuclear pore complex. Mol Cell. 2008; 30:721–31. [PubMed: 18570875]

23. Whittle JR, Schwartz TU. Architectural nucleoporins Nup157/170 and Nup133 are structurally related and descend from a second ancestral element. J Biol Chem. 2009; 284:28442–52. [PubMed: 19674973]

24. Choe S, Sun SX. The elasticity of alpha-helices. J Chem Phys. 2005; 122:244912. [PubMed: 16035821]

25. Devos D, et al. Simple fold composition and modular architecture of the nuclear pore complex. Proc Natl Acad Sci U S A. 2006; 103:2172–7. [PubMed: 16461911]

26. Melcak I, Hoelz A, Blobel G. Structure of Nup58/45 suggests flexible nuclear pore diameter by intermolecular sliding. Science. 2007; 315:1729–32. [PubMed: 17379812]

27. Shulga N, et al. In vivo nuclear transport kinetics in Saccharomyces cerevisiae: a role for heat shock protein 70 during targeting and translocation. J Cell Biol. 1996; 135:329–39. [PubMed: 8896592]

28. Brachmann CB, et al. Designer deletion strains derived from Saccharomyces cerevisiae S288C: a useful set of strains and plasmids for PCR-mediated gene disruption and other applications. Yeast. 1998; 14:115–32. [PubMed: 9483801]

29. Sheff MA, Thorn KS. Optimized cassettes for fluorescent protein tagging in Saccharomyces cerevisiae. Yeast. 2004; 21:661–70. [PubMed: 15197731]

30. Sherman F. Getting started with yeast. Methods Enzymol. 2002; 350:3–41. [PubMed: 12073320]

31. Frank J, et al. SPIDER and WEB: processing and visualization of images in 3D electron microscopy and related fields. J Struct Biol. 1996; 116:190–9. [PubMed: 8742743]

32. Pettersen EF, et al. UCSF Chimera--a visualization system for exploratory research and analysis. J Comput Chem. 2004; 25:1605–12. [PubMed: 15264254]

33. Elsliger MA, Wachter RM, Hanson GT, Kallio K, Remington SJ. Structural and spectral response of green fluorescent protein variants to changes in pH. Biochemistry. 1999; 38:5296–301. [PubMed: 10220315]

34. Maegawa Y, et al. Structure of the catalytic nucleotide-binding subunit A of A-type ATP synthase from Pyrococcus horikoshii reveals a novel domain related to the peripheral stalk. Acta Crystallogr D Biol Crystallogr. 2006; 62:483–8. [PubMed: 16627940]

35. Diepholz M, et al. A different conformation for EGC stator subcomplex in solution and in the assembled yeast V-ATPase: possible implications for regulatory disassembly. Structure. 2008; 16:1789–98. [PubMed: 19081055]

36. Shi J, Blundell TL, Mizuguchi K. FUGUE: sequence-structure homology recognition using environment-specific substitution tables and structure-dependent gap penalties. J Mol Biol. 2001; 310:243–57. [PubMed: 11419950]
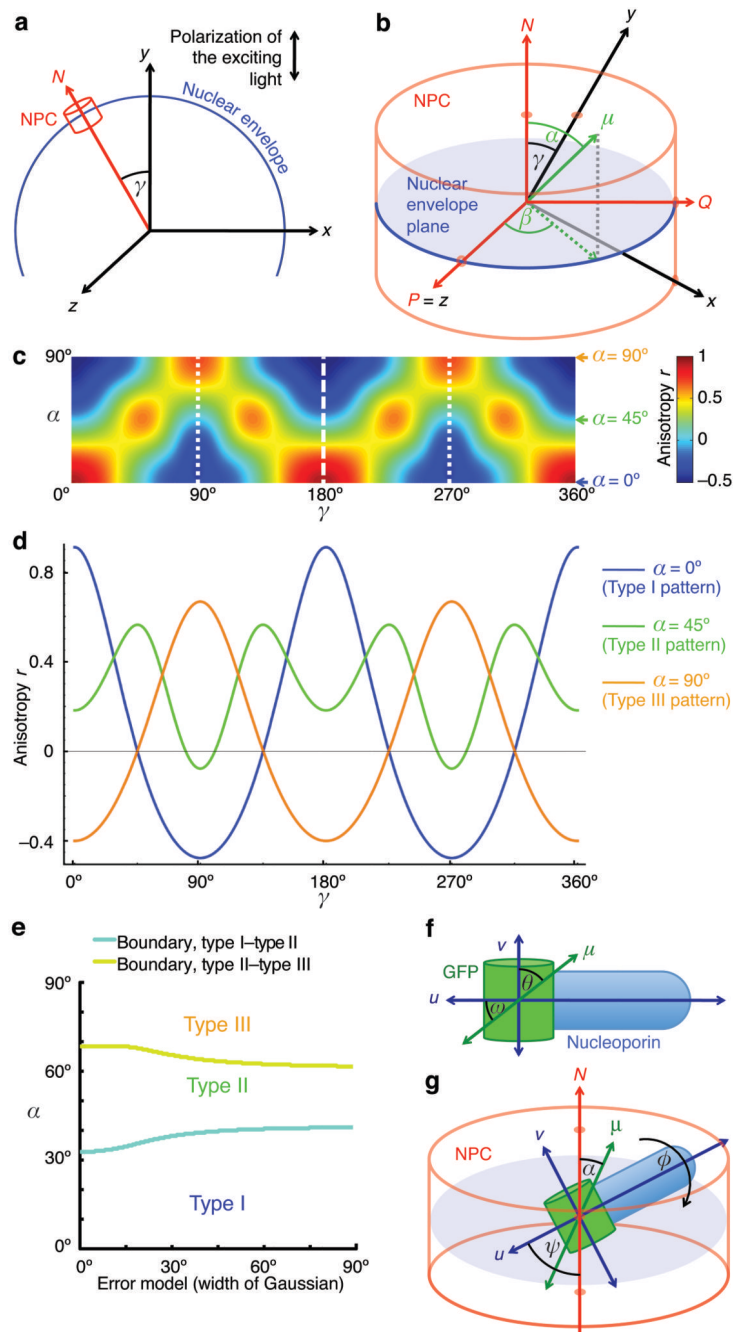
Figure 1.
Fluorescence anisotropy patterns reflect the orientation of fluorophores within the NPC. (**a**) A circular nuclear envelope cross-section seen in the microscope coordinate system *xyz*. The polarization direction of the exciting light is parallel to *y*. The object plane is defined by *xy*, the optical axis by *z*. The nucleocytoplasmic axis *N* of each NPC is perpendicular to the plane tangential to the point in nuclear envelope at which the NPC is located. The angle between the *y* axis and *N* at a given point in the nuclear envelope is defined as γ. (**b**) An individual NPC with its own coordinate system *NPQ*. *P* is chosen to coincide with the

optical axis z, PQ defines the nuclear envelope plane. The transition dipole of a fluorophore fixed within the NPC is μ. The orientation of μ within the NPC is described by α, the angle between μ and N, and β, the angle between P and the projection of μ onto the nuclear envelope plane PQ. (**c**) For a fluorophore with a given angle α, the anisotropy r can be predicted as a function of the nuclear envelope position γ. All functions $r(\gamma)$ have a period of 180° (dashed line) and have mirror symmetry axes (dotted lines). (**d**) Anisotropy patterns along the nuclear envelope cross-section are shown for three values of α that exemplify different pattern types, as defined in the text. (**e**) The values of α at which transitions between pattern types occur were plotted as a function of the width of the Gaussian function with which the theoretical anisotropy pattern was convoluted to approximate the effect of experimental factors on the measured anisotropy values (see Supplementary Note). (**f**) Two perpendicular axes, u and v, are arbitrarily defined within the nucleoporin. For a given nucleoporin–GFP construct, the angle between u and the fluorophore transition dipole μ is designated ω; the angle between v and μ is θ. (**g**) The orientation of a nucleoporin within the NPC is characterized by two parameters: ψ, the angle between u and the nucleocytoplasmic axis N, and ϕ, the angle of rotation around u.
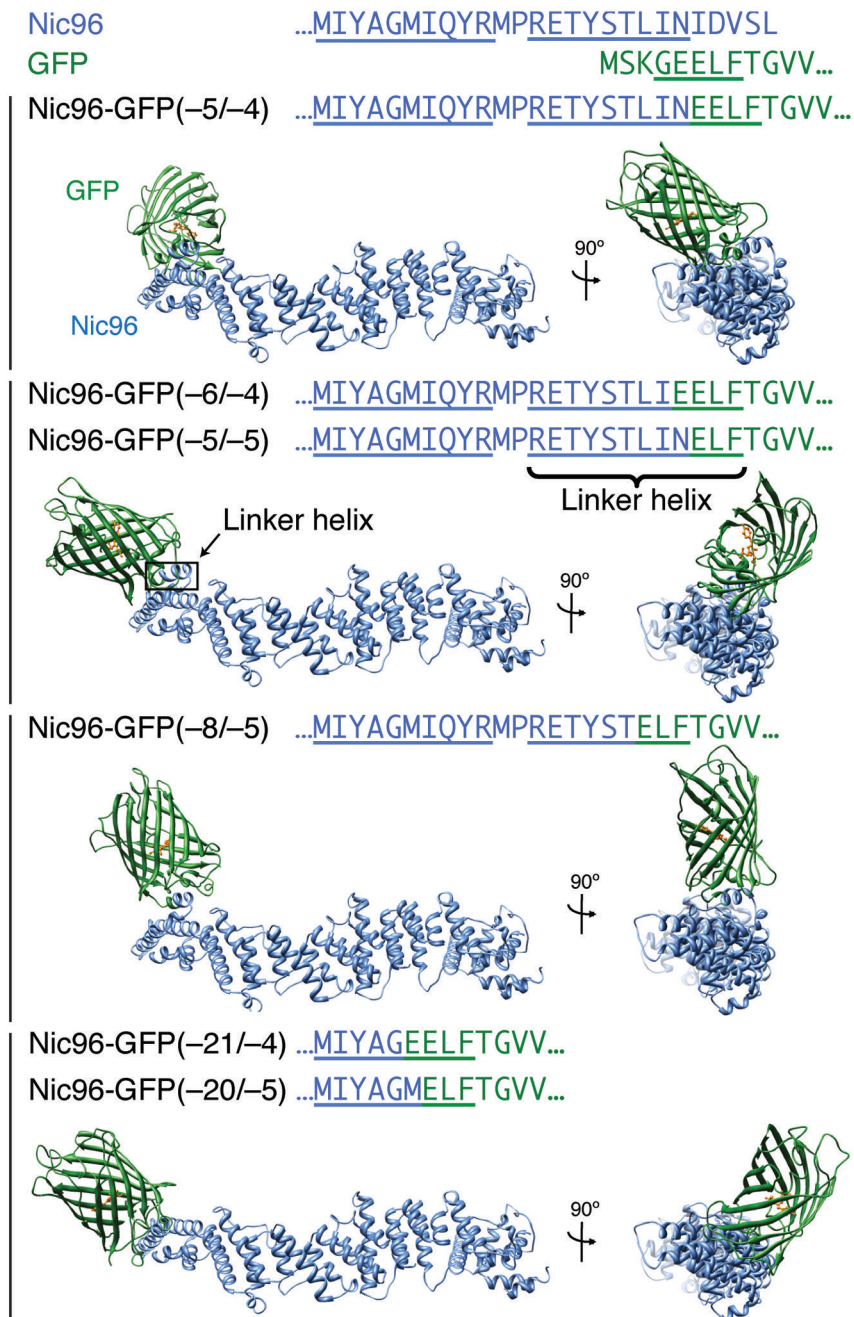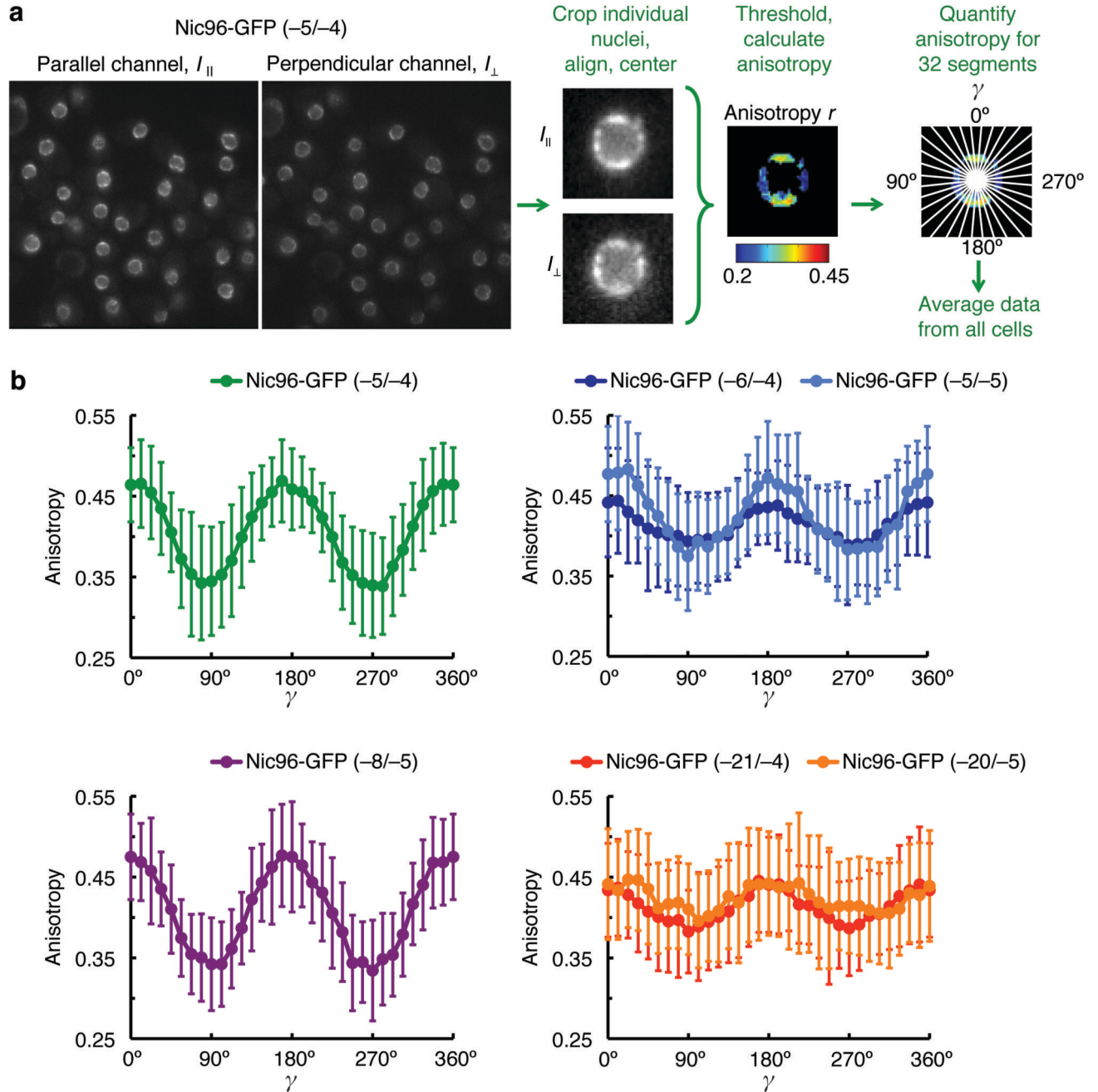
Figure 2.
Nic96–GFP constructs with a continuous linker α-helix. Sequences of the budding yeast Nic96 C-terminus (blue) and of the GFP N-terminus (green) are shown with α-helical segments underlined. The C-terminal α-helix of Nic96 can be fused to the N-terminal α-helix of GFP such that a continuous linker helix connects the two moieties. Models of fusion proteins based on crystal structures of Nic96 (light blue) and GFP (green, with fluorophore in orange) are shown.

Figure 3.
Polarized fluorescence microscopy reveals anisotropy patterns for yeast strains expressing Nic96–GFP constructs. (**a**) GFP-tagged yeast cells are excited with polarized light. Parallel and perpendicular components of the emitted light, $I_{\parallel}$ and $I_{\perp}$, are recorded simultaneously. Images of individual nuclei are cropped from the background-corrected micrographs and processed automatically as follows: $I_{\parallel}$ and $I_{\perp}$ images of the same nucleus are aligned and centered, and pixels not belonging to the nuclear envelope are masked by thresholding. An anisotropy image is calculated, and the average anisotropy is calculated within 32 sectors.
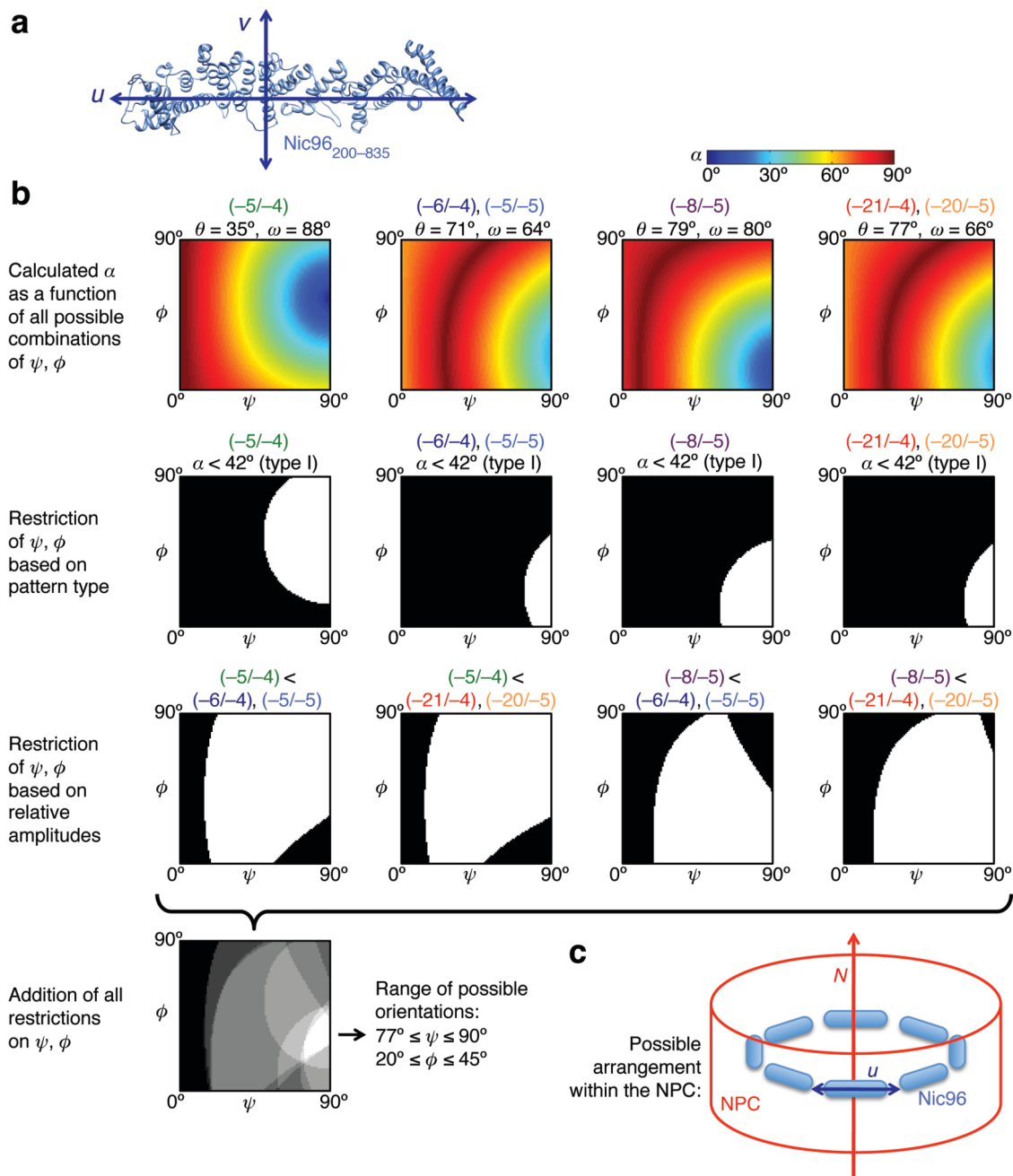
(**b**) Experimental anisotropy curves for six Nic96–GFP constructs. Error bars represent the standard deviation of average sector anisotropy values from individual cells.

Figure 4.
Analysis of anisotropy patterns reveals approximate orientation of Nic96 within the NPC.
(**a**) Two axes are defined with respect to the crystallized domain of Nic96: The long axis $\boldsymbol{u}$, and a perpendicular axis $\boldsymbol{v}$. (**b**) *First row*: For each Nic96–GFP construct, θ and ω are derived from the molecular model. a is calculated for all possible combinations of ψ and ϕ. *Second row*: The experimental anisotropy patterns (Fig. 3b) were all type I, corresponding to a value of $a < 42°$. Combinations of ψ and ϕ values satisfying this condition are shown in white; incompatible combinations of ψ and ϕ are shown in black. *Third row*: Since the

amplitude of type I patterns decreases as a increases between 0° and 42°, pairwise comparison of anisotropy curves with different amplitudes (Fig. 3b) further restricts the space of possible combinations of ψ and ϕ. *Last row*: All restrictions are combined to reveal the remaining space of possible ψ and ϕ values (white). (**c**) A value of ψ close to 90° is compatible with a published model[6] in which Nic96 molecules were proposed to form a ring with their long axis perpendicular to the nucleocytoplasmic axis, as shown schematically here.
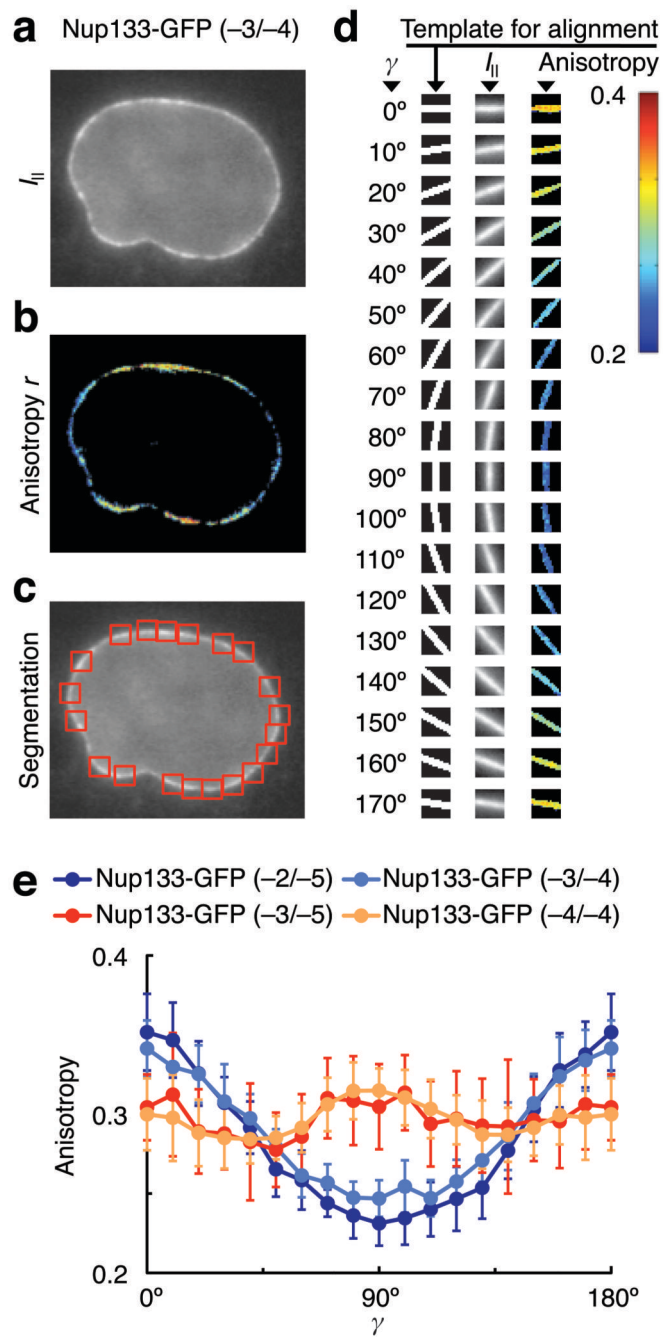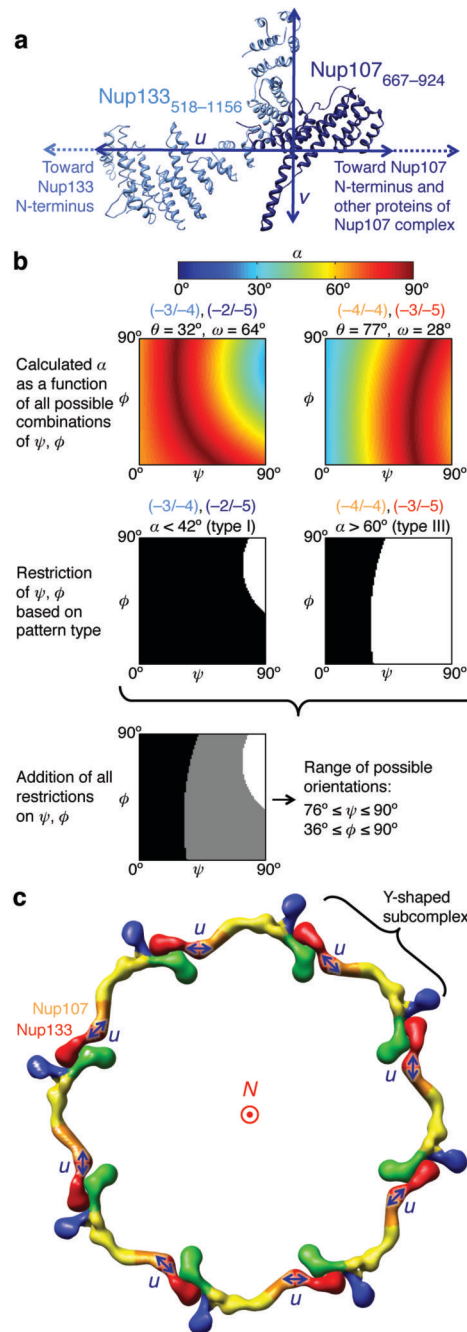
Figure 5.
Anisotropy patterns in mammalian cells expressing Nup133–GFP. (**a**) $I_{\parallel}$ image from polarized fluorescence microscopy of HeLa cell expressing Nup133–GFP (−3/−4). (**b**) Pseudocolored anisotropy image of the same cell. (**c**) 16×16 pixel boxes containing quasi-straight segments of nuclear envelope are selected. (**d**) Cross-correlation between the nuclear envelope segment and a series of template images is calculated to match the experimental image with the most similar template and thus determine the orientation of the nuclear envelope segment. *First column:* γ values. *Second column*: Corresponding synthetic

template images. *Third column*: Average $I_\parallel$ images of aligned segments from all Nup133–GFP (−3/−4) cells. *Fourth column*: Averaged anisotropy images of these segments. (**e**) Anisotropy curves obtained from segment analysis as outlined in (d), for 4 different Nup133–GFP constructs. Error bars represent the standard deviation of average segment anisotropy values from individual boxes.

Figure 6.
Nup133–GFP anisotropy patterns are consistent with the published "head-to-tail ring" arrangement of the Y-shaped subcomplex. (**a**) Two axes are defined with respect to the Nup133–Nup107 dimer: The long axis **u** connects the N-termini of the crystallized Nup107 and Nup133 domains, which connect to the remaining parts of the stem of the Y-shaped subcomplex. **u** should correspond approximately to the long axis of the entire subcomplex. The perpendicular axis **v** passes through the Nup133 C-terminus. (**b**) *First row*: For each Nup133–GFP construct, α was calculated for all possible combinations of ψ and φ. *Second*

and last row: For constructs (−3/−4) and (−2/−5), Type I anisotropy patterns were observed (Fig. 5e), indicating $\alpha < 42°$. For constructs (−4/−4) and (−3/−5), the Type III anisotropy patterns were observed (Fig. 5e), indicating $\alpha > 60°$. Combinations of ψ and ϕ compatible with these restrictions are shown in white. (**c**) The anisotropy data indicates that the angle ψ between $\boldsymbol{u}$, the long axis of the Nup107–Nup133 complex, and the nucleocytoplasmic axis $\boldsymbol{N}$ is closer to 90° than to 0°. This supports a model for the arrangement of the entire Y-shaped subcomplex in flat octameric head-to-tail rings. For illustrative purposes one such model was generated using the EM map of the homologous yeast Y-shaped complex and represents one subcomplex ring viewed along $\boldsymbol{N}$. Colors indicate building blocks of the Y-shaped subcomplex: additional details are given in Supplementary Figure 6.